Desalination and Water Treatment
www.deswater.com

doi: 10.5004/dwt.2019.23682

144 (2019) 243–256
March

A comparative study of two new CoZn nanoferrites: characterization, magnetic properties, and efficiency for the removal of hexavalent chromium from wastewaters

Lotfi Ben Tahar[a,b,c,*], Mohamed Habib Oueslati[a,d], Bilel Grindi[c,e]

[a]*College of Science of Arar, Northern Border University, P.O. Box 1231, Arar 91431, Saudi Arabia, Tel. +966 50 00 88 65 85/216 98 902 376; email: bentaharlotfi@gmail.com (L.B. Tahar), ouesmed74@gmail.com (M.H. Oueslati)*
[b]*Faculty of Science of Tunis, Tunis El Manar University, Campus Universitaire, 2092 Tunisia*
[c]*Université de Carthage, Faculté des Sciences de Bizerte, LR18 ES11, Laboratoire des composés hétéro-organiques et des matériaux nanostructurés, 7021, Zarzouna, Tunisie, email: billel.grindi@gmail.com*
[d]*Department of Chemistry, Preparatory Institute for Scientific and Technical Studies, Carthage University, P.O. Box 51, La Marsa 2070, Tunisia*
[e]*Toulouse University, LPCNO, INSA CNRS UMR 5215, 135 av. de Rangueil, 31077 Toulouse Cedex 4, France*

Received 29 September 2018; Accepted 25 December 2018

ABSTRACT

A new CoZn nanoferrite and its moderately calcined counterpart were produced by the polyol method aiming to assess their effectiveness for the removal of Cr(VI) species from aqueous solutions. The produced nanoparticles (NPs) were systematically studied by various techniques. X-ray diffraction revealed the formation of nanosized single-phase cubic spinel-type ferrites, and transmission electron microscopy showed the presence of almost ~10 nm sized spherical NPs. Magnetic study showed a superparamagnetic behavior at room temperature and a reasonable Curie temperature for both the as-prepared and calcined NPs. Adsorption study of Cr(VI) onto the moderately calcined NPs was carried out at pH 2.0. The uptake of the Cr(VI) was found to increase rapidly with the increase of the NP dose. Additionally, the adsorption of Cr(VI) onto the nanoferrite was found to follow a pseudo-second-order kinetics in agreement with a chemisorption process. Moreover, the equilibrium data points were found to follow the Langmuir isotherm model with an adsorption capacity of ≈16.0 mg g^{-1} for an adsorbent concentration of 4.0 mg mL^{-1}. The nanoadsorbent was also tested in ten adsorption–desorption–regeneration cycles without any significant loss in sorption capacity. All the features demonstrate that the moderately calcined CoZn ferrite is a promising nonmaterial for the treatment of chromium (VI)-bearing wastewaters.

Keywords: Nanoparticles; Ferrite; Magnetism; Chromium (VI); Removal; Regeneration

1. Introduction

Humanity is facing formidable challenges in meeting rising demands of supplies of freshwater [1,2]. Indeed, water quality is deteriorating continuously due to increasingly natural and man-made activities. There are various causes of water pollution related to human activities. They include industrial wastes, sewages, mining activities, chemical fertilizers and pesticides, radioactive waste, and so forth. In contaminated water, undesirable species can be broadly classified into three main categories, that is, organic compounds, microorganisms, and inorganic compounds (e.g., heavy metals, nitrates, sulfides) [3]. Water-soluble heavy metal (such as Hg, Cr, Cu, Cd, As, and Pb) chemicals are reported

---

* Corresponding author.

to be highly toxic to human, animals, plants, and more generally to the ecosystem [4]. Their toxicity depends on several factors including the dose, route of exposure, and the nature of chemical species, as well as the age, gender, genetics, and nutritional status of exposed individuals. Chromium (Cr) is one of the serious environmental pollutant [5–8]. In the environment, it exists most commonly as the trivalent (Cr(III)), hexavalent (Cr(VI)), and metallic (Cr(0)). Industrial processes generally produce Cr(VI) and Cr(0). Due to their high solubility, Cr(VI) species, particularly the chromates and the dichromates, are highly mobile in soil environments and water [8,9]. They are consequently considered to be the most toxic forms of chromium. Adverse effects of the hexavalent form on the skin may include ulcerations, dermatitis, and allergic skin reactions. Whilst, ingestion of these species by drinking contaminated water or breathing polluted air can cause serious health problems [9–11]. Besides, unlike the organic compounds, heavy metal species cannot be biodegraded or destroyed; therefore, they must be removed. To face real situations of the increasing water resource pollution, the removal of pollutants from contaminated water is an urgent need for providing disease-free health to our society and to the ecosystem; the adaptation of highly advanced nanotechnology to traditional process engineering would be of crucial importance in technological developments for water and wastewater treatment [12–14].

Because of its simplicity and relevancy to the industrial application, adsorption technique is increasingly used for the removal of water contaminants [15,16]. Ideally, the treatment of Cr(VI)-bearing wastes requires the removal of the heavy metal species followed by the safe recovery of both the adsorbent and the adsorbate. Nanoadsorbents have recently emerged as an alternative solution for conventional adsorbents [17,18]. Owing to their high surface area to mass ratio, dispersion ability, surface modifiability, tunable magnetic properties, biocompatibility, ease of decantation with the help of an external magnetic field, reusability, and cost effectiveness, spinel-type nanoferrite (with general chemical formula MFe_2O_4, where M is a simple bivalent cation such as Fe(II), Co(II), etc. or a combination of the cations)-based materials were reported to have immense potential for the adsorption and/or reduction of water-soluble heavy metals [19–24]. Recovery of the metals and other adsorbed species is also possible. We have recently reported the investigation of Cr(VI) removal using two magnetite derivatives; a magnetite-rich phase and a pure maghemite phase [25]. The pure maghemite nanoparticles (NPs) were found to have reasonable Cr(VI) removal capacity and enhanced kinetics (particularly in the case of low Cr(VI) concentrations) compared with conventional adsorbents such as activated carbon, alumina, zeolites, etc. The adsorption and the desorption efficiencies of a nanoadsorbent are controlled by various extrinsic physicochemical parameters [13]. The pH plays a pivotal role as it controls the surface charge density and thus the adsorption phenomenon and the surface complexation. For instance, for chromium (VI) species, it has been established that the maximum room temperature adsorption occurred in acidic medium at pH around 2.0 [26,27]. Indeed, at pH of 2.0–6.0, the predominant Cr(VI) species mainly exists in the $HCrO_4^-$ form, which is then gradually converted to CrO_4^{2-} form as pH increases [28]. Additionally, at acidic pH, the adsorption of the negatively charged chromate ions is due to the physical adsorption caused by electrostatic interaction with the positively charged protonated NP surface [29]. What is more, the adsorption free energy of $HCrO_4^-$ is notably lower than that of CrO_4^{2-} which makes $HCrO_4^-$ more favorably adsorbed. Therefore, the removal of Cr(VI) at lower pH around 2 is mainly due to the adsorption of $HCrO_4^-$. The aim of the present research work is to assess the potential capacity of two stoichiometric CoZn nanoferrites as adsorbents of Cr(VI) from aqueous solutions. One of the CoZn ferrites (the as-produced) was prepared by a one-pot coprecipitation synthesis using the polyol method [30]. The second ferrite was obtained by calcination of the former (the as-prepared) at 300°C for 24 h. The moderate calcination aims the removal of the chemisorbed organic species grafted onto the as-produced NPs while maintaining the structural, microstructural, and magnetic properties almost unchanged. The as-prepared NPs as well as their calcined counterparts were then systematically characterized for their chemical composition, phase purity, microstructure, thermal stability, and magnetic properties performing various techniques including energy-dispersive (EDX), X-ray diffraction (XRD), infrared (IR), thermogravimetric analysis/differential scanning calorimetry (TGA/DSC), ultraviolet-visible (UV-Vis), and vibrating-sample magnetometery (VSM). The effects of the adsorbent nature and dose, the contact time, and the Cr(VI) initial concentration at a constant pH (pH ~2) on the adsorption efficiency onto the two nanoferrites were then investigated. The investigation allowed us to select the best nanoferrite among the above-mentioned two ferrites for the removal of Cr(VI). Moreover, tests aiming the reusability of the selected nanoferrite were carried out.

2. Experimental procedure

2.1. NP synthesis

NPs with the nominal composition $Co_{0.6}Zn_{0.4}Fe_2O_4$ were prepared starting from the analytical grade precursor salts $Co(CH_3CO_2)_2{\cdot}4H_2O$ (Acros, Geel, Belgium, 97%), $Zn(CH_3CO_2)_2{\cdot}2H_2O$ (Fluka, St. Gallen, Switzerland, >99%), and $FeCl_3$ (Fluka, St. Gallen, Switzerland, 97%) using the polyol process according to the procedure described elsewhere [30]. The chemical composition, the stoichiometry, the structure, and the microstructure of polyol-made nanoferrites could be varied by controlling a number of physicochemical parameters: The reaction time, t, and the hydrolysis (h), the acetate (τ_{Ac}) and the Zn (τ_{Zn}) ratios, defined by the molar ratios water/metal, acetate/M^{2+}, and Zn^{2+}/Fe^{3+} (in the case of Zn-substituted ferrites) [31,32]. In the present chemical synthesis, values of t and τ_{Zn} were chosen equal to 4.0 h and 0.6, respectively, while the values of h and τ_{Ac} were imposed by the amounts of water and acetate ion of the different precursors and the anhydrous sodium acetate (Fluka, 99%). It is important to point out that for the purpose of comparison of Cr(VI) removal efficiency with the as-prepared nanoferrite, a given quantity of the last ferrite (namely, $Co_{0.6}Zn_{0.4}Fe_2O_4$) was calcined at 300°C for 24 h. The moderate calcination aims the removal of the grafted chemisorbed organic species without inducing any noticeable change on the structural, microstructural, and magnetic properties. The calcined NPs could lead to a better uptake efficiency of the Cr(VI) entities.

2.2. Characterization techniques

Phase purity, crystal structure, and microstructure of the produced powders were studied by XRD using an Empyrean X-ray diffractometer equipped with a cobalt anode ($\lambda_{CoK\alpha}$ = 1.789010/1.792900 Å). The XRD powder pattern indexing, the unit-cell constant calculation, and refinement were carried out by common crystallographic softwares [33–35]. The microstructure features were inferred from the diffraction peak broadening using the Williamson–Hall plots [36]. Mid IR characterization was carried out on a Nicolet UR 200 fourier-transform infrared spectroscopy apparatus. Elemental chemical analysis was conducted with an EDX Bruker Nano GmbH, Germany, detector mounted on a JEOL JSM-7800F scanning electron microscope (SEM). The particle morphology was observed by a JEOL JEM-1400 transmission electron microscope (TEM) operating at 100 kV. Particle size distribution was derived considering at least 200 particles measured on randomly chosen TEM micrographs. Thermal analysis (TGA/DSC) of the as-prepared powder was recorded in air with a flow rate of 50 mL min^{-1} and a heating rate of 10°C min^{-1} using a Mettler Toledo TGA/DSC 1 STAR. The magnetic measurements of the two ferrites under study were conducted on a Quantum Design PPMS VSM magnetometer. The hysteresis loops were measured with magnetic field cycling between +50 and −50 kOe at 5 and 300 K. Thermal variation susceptibility was measured in field cooling/zero field cooling (FC/ZFC) mode. In a typical measurement, for the ZFC experiment, the sample is cooled from room temperature to 5 K without any external magnetic field applied. Then, a magnetic field of 200 G is applied, and the magnetization is recorded as the temperature slowly rises to 300 K. The FC data are obtained by cooling the sample under the same magnetic field after the ZFC experiments and recording the change in net sample magnetization with temperature. The temperature-dependent magnetization was recorded in the temperature range 50–330 K under a fixed magnetic field of 20,000 Oe.

2.3. Batch adsorption experiments

For the room temperature investigation of the effect of a number of parameters including the nanoadsorbent dose, the contact time, and the Cr(VI) concentration on the adsorption, desorption, and regeneration capacity of the produced NPs, batch experiments were carried out at a fixed pH of ~2.0 in glass test tubes mounted with screw caps. The shaking was carried out with an ultrasonic shaker with intermittent vortexing. It is to be noticed that all chemical reagents used were of analytical grade or better and all aqueous solutions were prepared with ultrapure deionizer water (conductivity ≤ 40 µS cm^{-1}) by passage through a reverse osmosis water purification system (Pure Lab Prima, ELGA, UK). Further, all glassware was cleaned with 6.0 M HCl and then with ultrapure water before use. After adsorption, the adsorbents were separated from supernatant using a strong rectangular NdFeB (N40) magnet. The absorbance of the supernatant was then measured with a UV-Vis double-beam spectrophotometer (Jasco V-670) covering a wavelength range from 190 to 800 nm and equipped with 1-cm-wide quartz cells. For accurate determination of Cr(VI) concentration in the supernatants, a calibration curve was generated using a series of standard solutions of analytical grade potassium dichromate, $K_2Cr_2O_7$, (Sigma Aldrich, St. Louis, USA, ≥99%) dissolved in 0.01 M HNO_3 aqueous solution. The pH value was measured using a benchtop pH meter (Hach, Colorado, USA, SensION), and throughout the course of the experiments, the pH of each Cr(VI) solution (before the addition of adsorbent) was adjusted to the desired value (pH 2.0) using 0.1 HCl or 0.1 NaOH. UV-Vis absorbance values were recorded at the λ_{max} = 350 nm, and all the measurements were conducted in triplicate to ensure the accuracy, reliability, and reproducibility of the collected data. In order to recover the adsorbed Cr(VI) and to regenerate the adsorbent for further use, Cr(VI)-loaded NPs were dispersed in an excess of 0.5 M NaOH, and the mixture was sonicated for about 5 min. The liquid phase was then separated by magnetic decantation, and the NPs were thoroughly washed with distilled water until a neutral pH and then dried in an oven for their successive reuse as adsorbents for Cr(VI). The adsorption–desorption–regeneration cycle was repeated ten times aiming the assessment of the reusability of the produced NPs.

3. Results and discussion

3.1. Phase, structure, and thermal analyses

The elemental chemical composition and the preliminary morphological characterization of the as-produced ferrite were recorded on an SEM apparatus. EDX and elemental mapping analyses carried out at randomly selected areas of sample reveal the expected metallic elements, for instance, Fe, Co, and Zn. Fig. 1 provides an SEM image and the EDX spectrum of a selected zone of the as-produced sample. Further, it should be pointed out that close atomic ratios of the different chemical elements were found, indicating a high chemical homogeneity of the produced powder. Quantitative analysis inferred from EDX analysis permits the determination of the chemical formula of the as-produced ferrite, $Co_{0,6}Zn_{0,26}Fe_{2,09}O_4$. As can be clearly noticed, the chemical formula departs from this expected formula, $Co_{0.6}Zn_{0.4}Fe_2O_4$. The mixed ferrite shows a slight excess of Fe and a lack of Zn, while Co concentration agrees well with the expected nominal content. Such a result is not surprising; as already pointed out (section 2.1), the chemical composition depends strongly on various synthetic parameters. Particularly, it depends on the so-called hydrolysis ratio, Zn ratio, and acetate ratio. It is to be noted that the unassigned EDX peak with the lowest energy is attributed to carbon arising from both the sample holder and the small amount of organic entities grafted on particle surface (see IR characterization given below). Further, the organic entities are bearing C–O functional groups; therefore, they contribute by a small fraction to the oxygen content observed by EDX. In addition, from SEM images, the as-produced powder consists of agglomerated fine particles.

Clearly, it is difficult to determine the particle size performing SEM; therefore, TEM is necessary to determine the particle size and morphology of the fine particles. The XRD patterns of both the as-produced powders and their associated calcined ones at 300°C are shown in Fig. 2.

The observed diffraction lines are consistent with those of a typical spinel structure without evidence of impurities such as hematite and hydroxides. Additionally, for the as-produced ferrite, the determined cell parameter (Table 1) was found to

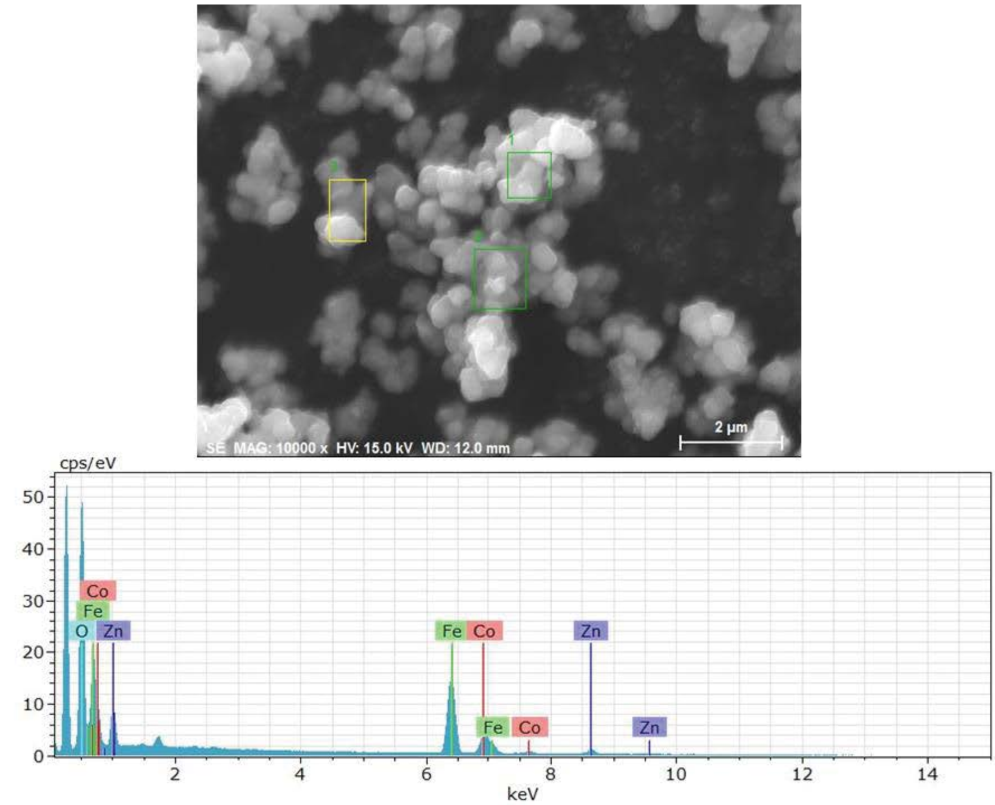

Fig. 1. A typical SEM image of the as-prepared CoZn ferrite powder with the EDX spectrum of selected zones. The unassigned EDX peak with the lowest energy is due to carbon arising from both the sample holder and a small amount of organic entities grafted on particle surface.

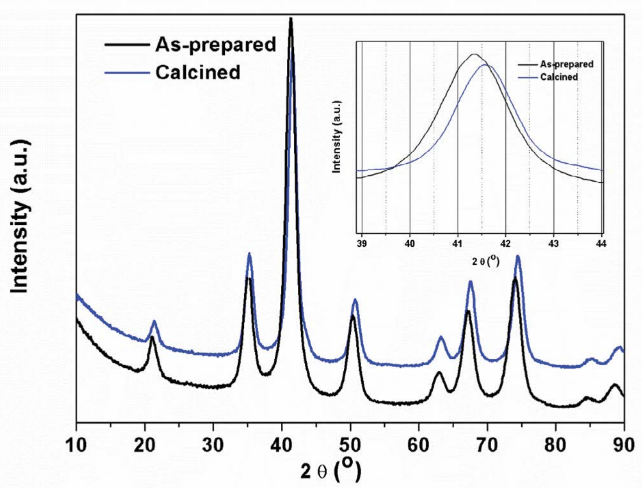

Fig. 2. XRD patterns of the as-prepared CoZn powder and its associated calcined one. The inset is a zoom view indicating the relative shift of XRD peaks as well as the intensity enhancement of the characteristic (311) peak.

be slightly smaller than that reported for the stoichiometric $Co_{0.6}Zn_{0.4}Fe_2O_4$ (8.416(7) Å) [37], thus supporting the Zn lack as inferred from EDX.

Besides, for the calcined ferrite counterpart, the cell parameter was found to be even slightly smaller than that of the as-prepared ferrite. A close examination of the XRD patterns reveals a little peak shift toward higher 2q for the calcined ferrite indicating reduction of the unit-cell parameter. As compared with the untreated ferrite, the cell parameter shrinkage observed for the calcined ferrite can be due to one or both the two factors: (i) It is well established that ferrite NPs exhibit metastable cation distribution among the tetrahedral (A) and the octahedral (B) sites [38,39]. The amplitude of deviation from the thermodynamically stable configuration (that of the bulk) depends on the elaboration conditions as well as the particle size. In the case of our calcined ferrite, a long-time calcination seems to bring sufficient energy to the spinel-type network allowing partial cation rearrangement between the spinel sites, namely, the B and the A sites, thus giving rise to more thermodynamically stable configuration. Given the fact that Zn^{2+} ions have strong preference for occupying the tetrahedral (A) sites in Zn-substituted ferrites [39], the cation rearrangement in our case should imply the remaining two cations, namely, Co^{2+} and Fe^{3+} ions. The cation rearrangement leads to a modification in the unit-cell parameter due to its dependence on the complex interplay between the size of the ions and their distribution. (ii) The unit-cell parameters of most nanocrystalline materials can also be significantly different from the coarse grain or single-crystal counterparts due to the grain surface relaxation effect [38]. The IR spectra of both the as-synthesized ferrite and its calcined counterpart are shown in Fig. 3.

The spectra can be viewed as divided into three regions: (i) A low-frequency region (~400 to 700 cm^{-1}) which exhibited the

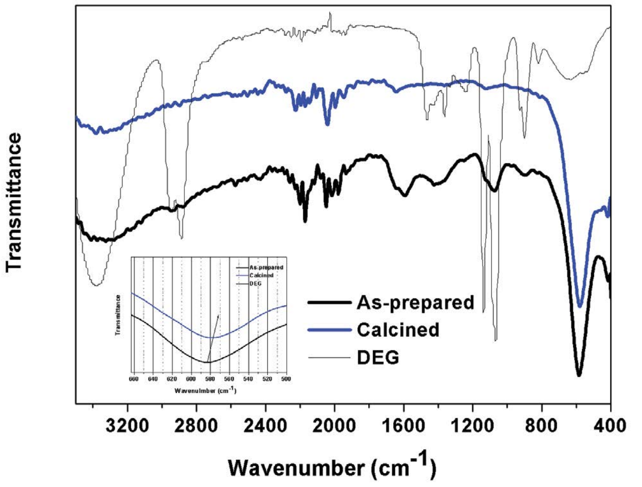

Fig. 3. IR spectra of the as-prepared CoZn ferrite and its associated calcined one. The IR spectrum of the polyol (DEG).

spinel-type ferrite features [40]. A very intense band located at ~580 arising from lattice vibrations was associated to the vibration of oxide ions against the cations ($\nu Fe_A\cdots_O$ (usually denoted as ν_1)) located in the tetrahedral (A) sites. A close look at the IR spectra (see the inset in Fig. 3) revealed a slight difference (6 cm^{-1}) in the ν_1 position of the two ferrites. This can be correlated to a slight variation in the tetrahedral $r_{A\text{–}O}$ bond length (defined as the average cation oxygen bond length on A sites) consequence of a probable tetrahedral site occupancy variation due to thermal treatment. The interpretation deduced from IR analysis supported the possibility (i) made on the basis of XRD. (ii) A medium frequency region (~1,000 to 1,600 cm^{-1}) showing the features of the polyol and acetate species grafted onto the surface of NPs; for the untreated particles, for instance, two bands located at ~1,420 and 1,590 cm^{-1} are assigned to the symmetric and asymmetric stretching vibrations of acetate ions, respectively, whereas the other two bands in the range 1,050–1,150 cm^{-1} are due to the C–O–C/C–O elongations. These assignments are supported by the presence of very weak couple of sharp bands located at ~2,920/2,880 cm^{-1} associated with asymmetric/symmetric C–H stretching vibrations. It is noteworthy that for the calcined ferrite, the intensities of the IR bands associated to the organic entities are notably weakened indicating that they are nearly completely removed from the surface of the NPs. (iii) A high-frequency region (over 3,000 cm^{-1}) showing a broad band centered at ~3,350 is associated with the O–H stretching of water molecules and the hydroxyl ions (OH–) of the alkaline reaction medium. Here again, in the case of the calcined ferrite, the weakening of the IR bands associated with O–H stretching indicates the departure of the major water molecules and the hydroxyl ions on heating. Thermal behavior of the as-produced powder was studied by TGA/DSC and IR. The TGA/DSC curves (Fig. 4) revealed a slight initial endothermic mass loss up to 150°C due to the removal of adsorbed water.

After this, an important mass loss in the ~150°C to 500°C range accompanied by an exothermic effect attributed to the combustion of the organic entities (polyol and acetate) chemisorbed on the surface of the NPs occurs. The last result is supported by the IR study given before. The organic species form strong chemical bonds with the metallic ions, since their complete removal is accomplished at relatively high. The interpretation is proved by the complete disappearance of the IR features of the mentioned chemical species, namely, the organic and hydroxyl groups from the IR spectra (not shown) of samples calcined at temperatures above 500°C. Additionally, the absence of any detectable thermal effect beyond 500°C indicated high thermal stability of the CoZn ferrite.

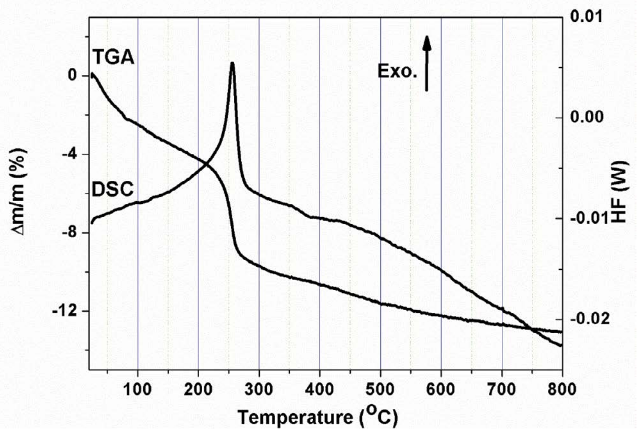

Fig. 4. TGA/DSC thermograms of the as-prepared CoZn ferrite.

3.2. Microstructural analysis

For both the as-produced and moderately calcined powders, the XRD peaks showed a clear broadening (with a slight less broadening for the calcined powder as can be observed from the zoom view around the intense peak), as a result of the reduced particle size and/or lattice strain. W-H plots are shown in Fig. 5, and the calculated crystallite size (<L_{XRD}>) and lattice strain (ε) are listed in Table 1.

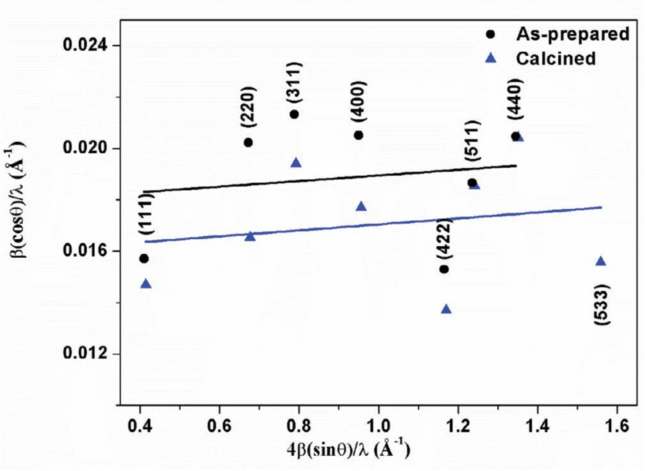

Fig. 5. W-H plots of the as-prepared and calcined powders. The straight lines are the fits to the data points.

Table 1
Selected structural (the lattice parameter (a) and the lattice mode (ν_1) associated to the vibration of oxide ions against the cations in A sites) and microstructural characteristics (the average crystallite size ($<L_{XRD}>$) and the strain (ε) inferred from XRD analysis and the average particle size ($<D_{TEM}>$) inferred from TEM analysis) of both as-prepared and calcined ferrites

	a, Å	$<L_{XRD}>$, nm	ε, %	$<D_{TEM}>$, nm	ν_1, cm^{-1}
As-prepared	8.407 (4)	5.6	0.109	10 ± 2	584
Calcined	8.387 (2)	6.3	0.116	11 ± 2	578

Both the crystallites, as-prepared and calcined ferrites, are ultrafine with an average size of about 6 nm. Besides, as expected, the crystallites of the calcined powder are slight larger due to the moderate heating. For both powders, the lattice strain values are very low in accordance with the good crystallinity known for the polyol-made ferrite NPs [31,37]. Morphology of both as-prepared and calcined NPs, along with their size distribution histogram, is evaluated with TEM analysis, and the results are presented in Fig. 6 and Table 1.

Some agglomeration is observed from the micrographs, which may be due to the sample preparation. Grains of both powders are observed to have nearly spherical morphology with an estimated average size of ~10 and 11 nm for the as-produced and the calcined samples, respectively. Additionally, grain size estimated from TEM is in reasonable agreement with the crystallite size revealed from W-H analysis using XRD (~6 nm), which may reveal nearly single crystalline character of NPs of the two ferrites. From the analysis, it is clear that the influence of calcination at 300°C on the microstructure of the as-produced NPs was insignificant. Calcination was just applied to remove the chemisorbed organic species from the NP surface.

3.3. Magnetic study

The magnetic susceptibility measurements of the two nanoferrites clearly show their dependence on the temperature and the type of NPs (Fig. 7).

In the ZFC regime, the magnetic susceptibility (χ) initially increases and reaches a maximum at a certain temperature. The temperature, at which the maximum susceptibility is achieved, is defined as the average blocking temperature, T_b of the nanoparticulate sample. T_b represents the threshold temperature above which magnetic anisotropy barrier is overcome by thermal activation energy alone, causing NPs to relax from the ferrimagnetic state to the superparamagnetic state. T_b values listed in Table 2 are lower than 300 K indicating a superparamagnetic behavior at room temperature. Additionally, for both nanoferrites, the ZFC and FC curves

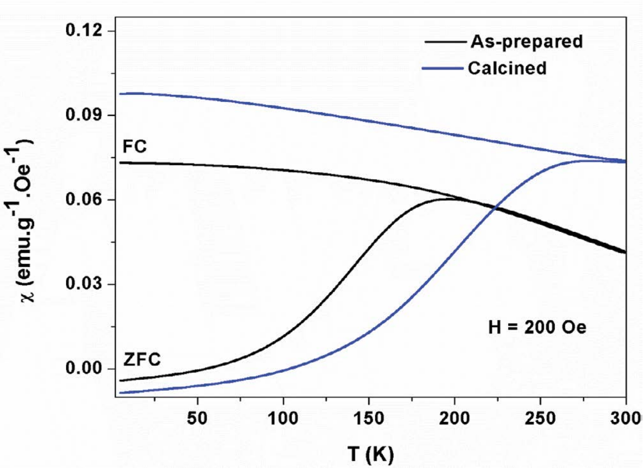

Fig. 7. FC/ZFC thermal variation of the susceptibility measured in a magnetic field of 200 Oe for the as-prepared CoZn ferrite NPs and their associated calcined ones.

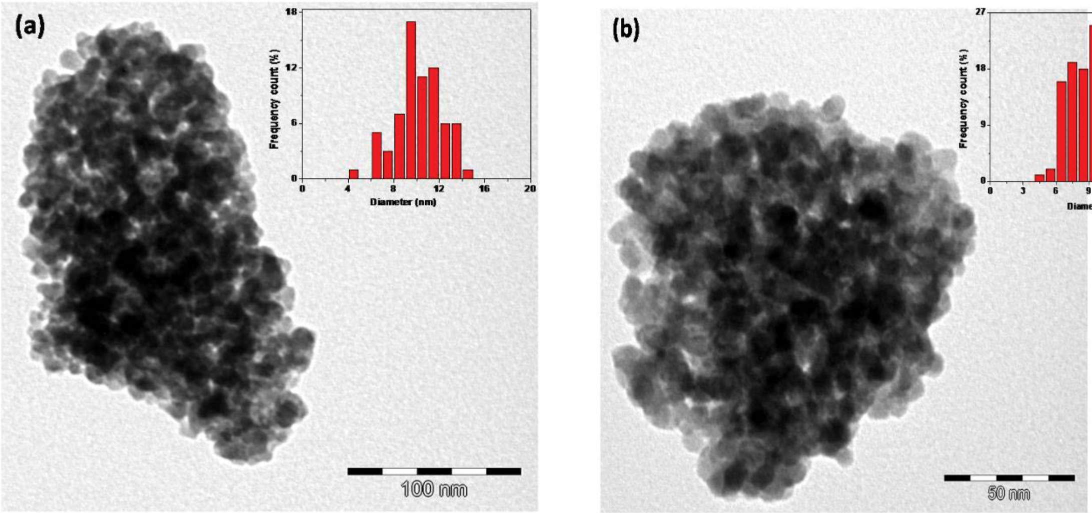

Fig. 6. Typical TEM images of the as-prepared CoZn ferrite powder (a) and its calcined counterpart (b) with their corresponding particle size distribution histograms.

Table 2
The main magnetic characteristics (the blocking temperature (T_b), the saturation magnetization measured at 300 K (M_{sat} (300 K)), the saturation magnetization measured at 5 K (M_{sat} (5 K)), the coercive field measured at 5 K (H_c (5 K)), the Curie temperature (T_C), the Bloch's exponent (β), and the spontaneous magnetization at 0 K (M (0))) of both as-prepared and calcined ferrites

	T_b, K	M_{sat} (300 K), emu g^{-1}	M_{sat} (5 K), emu g^{-1}	H_c (5 K), Oe	T_C, K	β	M (0), emu g^{-1}
As-prepared	197	69.5	96.7	6,157	644	1.66	86.3
Calcined	278	63.8	93.7	7,568	734	1.21	78.5

diverge at temperatures around T_b. The divergence is a characteristic feature of superparamagnetic behavior [41]. Further, the closeness (~10 K) of the blocking temperature and the temperature of the ZFC/FC curve separation indicate the presence of NPs with a narrow size distribution [42].

In addition, the relatively large ZFC curves around T_b is a consequence of the occurrence of interparticle magnetic interaction. As can be noticed from Table 2, the T_b value of the calcined ferrite is clearly larger (+91 K). Despite the occurrence of interparticle magnetic interaction, the difference in T_b values between the two ferrites can be approximately interpreted on the basis of the Stoner-Wohlfarth theory of a given noninteracting isotropic and randomly distributed magnetic uniaxial single domains (NPs) [43]. Indeed, the extrinsic magnetic contribution (interparticle magnetic interaction) to the T_b value is expected to be similar in both ferrites since their powders contain NPs of almost equal size and can therefore be ignored in the explanation of the difference of T_b between the two materials. According to the Stoner-Wohlfarth theory, T_b is proportional to the product of the so-called monocrystalline anisotropy, K_u, and the average particle volume, V:

$$K_u V \approx 25 k_B T_b \tag{1}$$

where k_B denotes the Boltzmann constant.

According to Eq. (1) and taking into consideration that the particle size remains almost constant after calcination, V, of the two nanoferrites, the notable difference in blocking temperature is likely to be mainly ascribed to the difference of intrinsic parameter K_u between the ferrites. The monocrystalline anisotropy value certainly depends on the cation distribution over the spinel sites, which differ significantly between the as-produced ferrite and the calcined counterpart as demonstrated above (see section 3.1). In ferrites containing cobalt ions, K_u is large due to the occurrence of a strong spin-orbital coupling for the octahedrally coordinated Co^{2+} ions [44]. Therefore, the larger T_b value observed for the calcined ferrite is probably due to the migration of a fraction of Co^{2+} from tetrahedral (A) to octahedral (B) sites accompanied by an opposite transfer of an equivalent number of Fe^{3+} ions from octahedral to tetrahedral sites, thereby increasing the concentration of Co^{2+} in B sites and leading finally to the enhancement of K_u. This result corroborates the results deduced form XRD and IR interpretations suggesting the variation in the cations distribution of the as-produced ferrite upon calcination. Magnetization as a function of the magnitude of an external dc applied field, H at the temperatures 300 and 5 K, was recorded for both the as-prepared and calcined ferrites (Fig. 8).

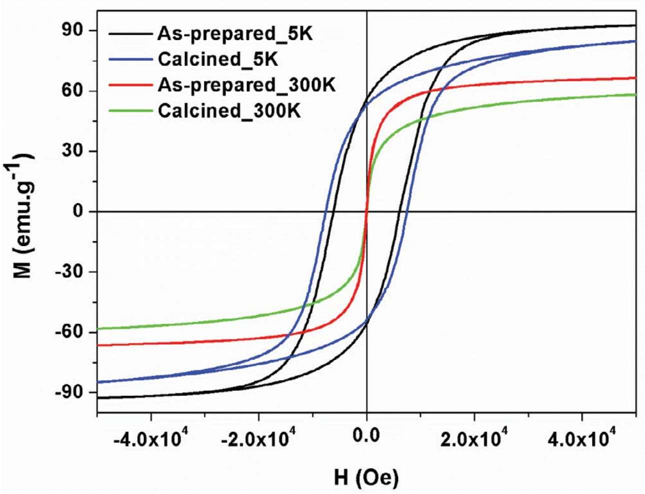

Fig. 8. Hysteresis loops measured at 5 and 300 K for the as-prepared CoZn NPs and their associated calcined ones.

As expected at 300 K (above T_b), there is no hysteresis features, in agreement with the superparamagnetic behavior of the particles. On the other hand, below T_b (for instance, at 5 K), a hysteresis loop is clearly observed for the as-prepared samples, in agreement with a blocked state of individual magnetic moments at 5 K. The saturation magnetization, M_{sat}, values determined by extrapolating the magnetization vs $1/H$ curve to $1/H = 0$ are given in Table 2. For the as-produced NPs, M_{sat} values are slightly larger than that of the calcined ferrite. In addition, the lower M_{sat} values measured at 300 K are due to the thermal fluctuation of the magnetic moments of superparamagnetic particles. For the as-prepared nanocrystals, below T_b, the reduced remanence, M_{rem}/M_{sat}, defined by the ratio of the saturation magnetization to the remanence magnetization, is close to 50%. The result is in agreement with the features of single-domain NPs with randomly oriented uniaxial anisotropy [44]. In nanoferrites with the same chemical composition, two factors are expected to affect the magnetization: (i) the particle size and (ii) the cation distribution. It is well established that the magnetization increases with the increase of particle size [32,41], while the second parameter (ii) could either increase or decrease the magnetization depending on the magnetic configuration and the site occupancy of the cations over the spinel sites, namely, the tetrahedral (A) and the octahedral (B) sites. In our case, magnetization of the calcined ferrite is found to be noticeably lower than that of the as-produced ferrite; the parameter (ii) is therefore expected to largely compensate the expected slight increase of the magnetization due to particle size increase. Considering the values of magnetic moments of the octahedrally coordinated high-spin Fe^{3+} and Co^{2+} cations of ~5 and ~4 μ_B (where $\mu_B = 9.274 \times 10^{-24}$ J T^{-1}), respectively [45], and considering the Néel model of ferrimagnetism [46], the plausible explanation of the magnetization decrease in the calcined ferrite compared with the as-synthesized one is the occurrence of a migration of a fraction of Co^{2+} from tetrahedral to octahedral sites accompanied by an opposite transfer of an equivalent number of Fe^{3+} ions from octahedral to tetrahedral sites. It is should be noted here that the interpretation corroborates with the last interpretation dealing with the increase of the magnetic anisotropy, K_u, upon calcination. The coercivity of the calcined ferrite (7,568 Oe) is much larger than that of the as-prepared ferrite (6,157 Oe). The coercivity of magnetic nanocrystals is surely related to the magnetic anisotropy [44]. At a given temperature, the required magnetic field strength for overcoming anisotropy to flip the magnetic spin certainly increases with increasing anisotropy energy barrier. The higher the Co^{2+} concentration in B sites, the stronger the L–S couplings in Co^{2+} cations and therefore the higher the coercivity. It has to be noted that here again the interpretation confirms the interpretations given before for T_b and M_{rem}/M_{sat}. Decay of magnetization with temperature of spinel ferrites is an important feature of magnetic materials from the point of view of technological applications. To get a quantitative description, we measured the temperature dependence of the magnetization, M, of the two materials submitted to a magnetic field of 20 kOe strength (Fig. 9).

For nanostructured ferrites, below the Curie temperature, M vs T, data points can be well fitted with a modified Bloch's law function [47]:

$$M(T) = M(0)\left[1 - \left(\frac{T}{T_c}\right)^{\beta}\right] \qquad (2)$$

where M (0) is the spontaneous magnetization at 0 K, T_C is the Curie temperature, and β is the so-called Bloch's exponent. M (0) and T_C values correspond to the intercept of the modified Bloch's law curves with the M_{sp} (T) and T axis, respectively. An excellent fitting with a modified Bloch's was obtained. The modified Bloch's law parameters are gathered in Table 2. T_C value of the calcined sample was found to be notably larger (90 K) than the Curie temperature of that of the as-produced counterpart. In spinel ferrites, Curie temperature (T_C) depends on the respective exchange integrals of the A–B and B–B interactions, with A–B interaction larger than A–A and B–B interactions in the order A–B > B–B >> A–A [48]. It is mostly controlled by super-exchange interactions between the Fe^{3+} ions in A and B sites. This strength of the A–B interaction is determined by the number of Fe_A^{3+}–O–Fe_B^{3+} linkages per magnetic ion per formula unit. Hence, the T_C depends on the number of linkages per Fe^{3+} ion per formula unit. In the case of our ferrites, the larger T_C value of the calcined compared with the as-prepared ferrite traduces an increase of Fe^{3+} population in A sites leading to increase of Fe_A^{3+}–O–Fe_B^{3+} interactions. Here again, the interpretation corroborates the interpretations given for changes observed for the above-cited magnetic parameters, namely, T_b, M_{sat}, and H_c. All the results demonstrate the occurrence of an exchange of fraction of Fe^{3+} and Co^{2+} over A and B sites upon calcination. The Bloch's exponent values are in agreement with previous reports for other spinel ferrites [49]. Additionally, as can be noticed from Fig. 9, the magnetization decay rate is low which allows the materials to maintain reasonable magnetization in a large temperature range. The Curie temperature (Table 2) of both ferrites exceeded 350°C, which favorites the two materials to work even under severe conditions (for instance, in contact with hot wastewaters) while maintaining a good interaction with an external magnetic field to perform their decantation easily.

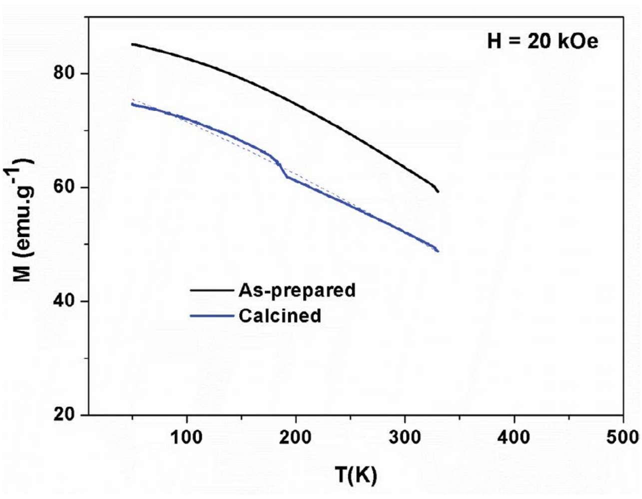

Fig. 9. Spontaneous M vs T measured at 20 kOe for the as-prepared CoZn NPs and their associated calcined ones.

3.4. Removal essays of Cr(VI)

In each Cr(VI) removal essay, a certain amount of the ferrite NPs (0.5–2.0 mg mL^{-1}) was added to a given volume of the hexavalent chromium acidic aqueous solution (pH ~2.0) having a precise Cr(VI) concentration (10–200 mg mL^{-1}). Each mixture was then vigorously stirred at room temperature for a certain time (10–240 min) with the assistance of ultrasonication/vortexing. Then, the supernatant is separated from the nanoadsorbent, and its absorbance was then measured using UV-Vis spectroscopy.

3.4.1. Effect of NP nature

Preliminary assessment of the removal ability of our NPs, namely, the as-prepared and the calcined CoZn ferrites in an acidic medium of pH 2.0, is of importance for an economical point of view. In a typical procedure, 60.0 mg of each ferrite was accurately weighted. Then 10 mL of a 50 mg L^{-1} Cr(VI) solution was added to the weighted NPs. After this, the mixture was shaked at room temperature for 25 min, and then the liquid phase was quickly separated from the solid phase with the help of a strong NdFeB magnet. Finally, the UV-Vis spectrum of the supernatants was recorded against an HNO_3 solution of pH 2.0 as a blank. Fig. 10 compares the UV-Vis spectra of the untreated Cr(VI) solution with its associated solutions treated by the as-prepared and the

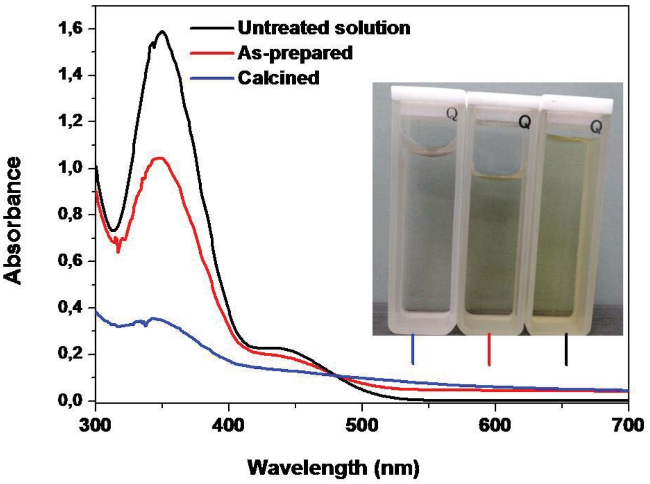

Fig. 10. The UV-Vis spectra of 50 mg L^{-1} Cr(VI) solutions treated by 6 mg L^{-1} of the as-prepared and 6 mg L^{-1} of the calcined CoZn NPs for a contact time of 25 min along with the untreated Cr(VI) solution. The inset depicts photos of the corresponding supernatants.

calcined NPs. As can be clearly seen, the intensity of the characteristic peak of Cr(VI) species at 350 nm decreased significantly in the presence of the as-prepared NPs and more sharply in the presence of the calcined ferrite. Certainly, the decrease in absorbance indicates a decrease in Cr(VI) concentration consequence of adsorption of a certain quantity of the species onto the NPs. A photo of the three solutions (see the inset in Fig. 10) shows a notable decrease of the characteristic yellow color of $K_2Cr_2O_7$ solution in the presence of the as-prepared adsorbent, while the supernatant becomes almost colorless in contact with the calcined NPs, thus supporting the trend of the intensity of the characteristic peak at 350 nm. From the preliminary study, it is clear that the calcined NPs showed superior efficiency toward Cr(VI) uptake; we therefore discarded the as-prepared NPs, and hereafter we focused only on the study of the adsorption of Cr(VI) species by the calcined NPs. A plausible explanation of the higher uptake efficiency observed for the calcined NPs is that for these NPs a larger number of positively charged surface sites are exposed to the negatively charged Cr(VI) species consequence of the removal of the organic species, namely, the polyol and the acetate ions upon calcination. In the case of the as-prepared NPs, however, the organic species possessing hydrophilic tails appear to exert a steric repulsion preventing an ease electrostatic attraction of the $HCrO_4^-$ ions toward the NP surfaces.

3.4.2. Effect of NP dose

Different amounts (0.6–4.6 g L^{-1}) of nanoadsorbents were suspended in 10 mL of 20 mg L^{-1} Cr(VI) solution under pH ~2.0 and for a contact time of 1 h. Fig. 11 shows the effect of adsorbent dose on the absorbance spectra of band of Cr(VI) solutions.

It can be seen that the intensity of the characteristic absorbance band of Cr(VI) species decreased drastically with the increase in NP dose indicating an important decrease of Cr(VI) concentration with the increase in the amount of NPs.

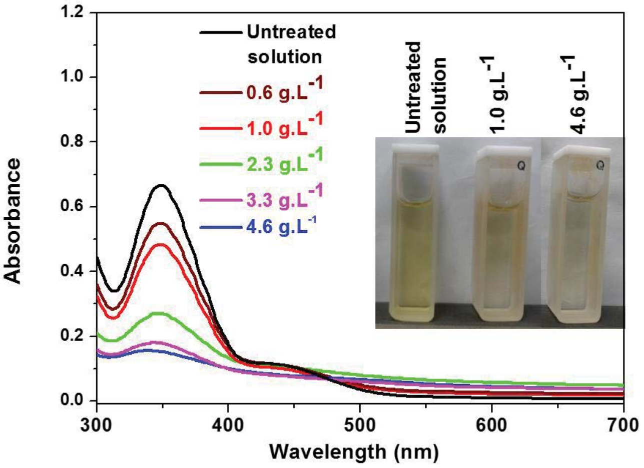

Fig. 11. Absorption spectra of 10 mL of 20 mg L^{-1} Cr(VI) solution treated with different doses of the calcined ferrite NPs. The inset depicts selected photos of the treated solutions in comparison with the untreated solution.

Based on the calibration curve and the absorbance values measured for the treated solutions, it is possible to deduce the removal percentage of Cr(VI) after 1 h of contact:

$$\text{Removal}(\%) = \frac{C_0 - C_{1\text{hr}}}{C_0} \times 100 \tag{3}$$

where C_0 and $C_{1\text{hr}}$ are the concentrations of Cr(VI) (mg L^{-1}) before (t = 0) and after 1 h of contact with the ferrite NPs, respectively.

Removal percentage as a function of selected adsorbent dose is presented in Fig. 12. It is obvious that NP dose affected the adsorption remarkably.

With the increase of the adsorbent quantity, the removal percentage begins to increase rapidly and then increases slowly to finally reach an almost constant value for high doses. As an example, the removal of 10%, 50%, and 80%

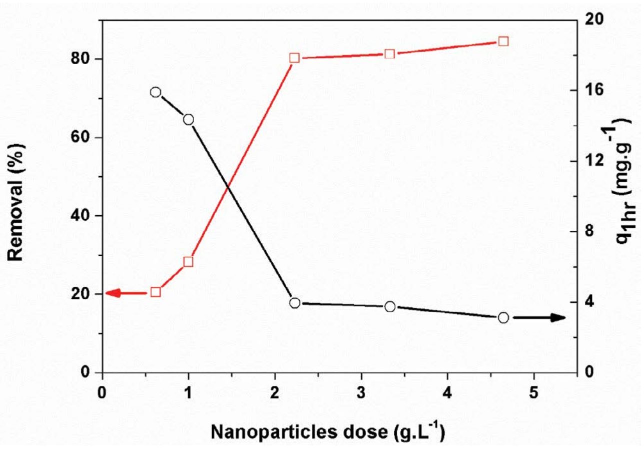

Fig. 12. Removal percentage and adsorbed quantity (mg g^{-1}) of 10 mL of 20 mg L^{-1} Cr(VI) solution treated with various doses of calcined ferrite NPs.

of Cr(VI) occurs for NP doses of ≈1.0, ≈2.5, and ≈3.9 g L^{-1}, respectively. The trend can be explained as follows: For a fixed number of Cr(VI) species, the increase of sorbent NPs means an increase of NP surface area, thus giving larger number of adsorption active sites and therefore high removal percentage of Cr(VI). For higher adsorbent doses and for a sufficient contact time, the available Cr(VI) species can be totally consumed by the NPs and the removal percentage attains its maximum value of 100%. For a given number of adsorbate species, the removal increase can be explained by the fact that the increase of sorbent NPs leads to surface area increase, thus giving larger number of adsorption sites and therefore larger number of adsorbed Cr(VI) species [50]. Removal capacity for an hour of contact can be evaluated in milligrams of the Cr(VI) species adsorbed by a gram of NPs:

$$q_{1\mathrm{hr}} = \frac{C_0 - C_{1\mathrm{hr}}}{m_{\mathrm{NPs}}} \times V \tag{4}$$

where $q_{1\mathrm{hr}}$ is the adsorption amount (mg g^{-1}) and C_0 and $C_{1\mathrm{hr}}$ are the same as those defined before. V is the volume of supernatant (L) and m_{NPs} is the mass of NPs used (g). $q_{1\mathrm{hr}}$ values vs adsorbent quantity are presented in Fig. 12. As the dose of the adsorbent increases, the adsorbed Cr(VI) quantity decreases with an almost monotonous manner but with a much rate for the low NP dose. The removed quantities for the lowest (0.6 g L^{-1}) and the highest (4.6 g L^{-1}) doses are ~16 and 3 mg g^{-1}, respectively. Similar trends regarding the removal percentage and the adsorption capacity were observed by Gupta and Rastogi in their study of the removal of Cr(VI) by the biosorbent *N. muscorum* [51] and Tahar et al. in their study of the removal of Cr(VI) by maghemite NPs [25]. For a given adsorbate quantity, aggregation caused by Van Der Waals due to high surface to volume ratio and by the magnetic interactions between NPs is a plausible explanation of a such trend in adsorption yield. The higher the quantity of the NPs, the higher the physical interactions and thereby the higher agglomeration degree, leading to the decrease of the screened fraction of the adsorbing active sites.

3.4.3. Kinetics study

In addition to sorption affinity, it is important that the magnetic NPs achieve rapid sorption to minimize the time required to remove cations. A 7.5 mL of 10, 20, 30, 40, 50, 60, 80, and 100 mg L^{-1} Cr(VI) solutions and a fixed quantity of NPs (4.0 g L^{-1}) were shaked at pH 2.0 at room temperature at various contact times, and their UV-Vis spectra were then recorded. The effect of contact time on the rate and the removal efficiency of Cr(VI) is shown in Fig. 13 for different initial concentrations of Cr(VI).

The removal percentage of Cr(VI) was calculated applying Eq. (4) for any time t. It can be seen that the rate of Cr(VI) uptake takes place in two phases: An initial phase involving rapid uptake of metal species, followed by a subsequent much slower removal rate leading gradually to an equilibrium state. For all concentrations, more than 50% of the removal of Cr(VI) takes place during the first 5 min. The rapid adsorption of Cr(VI) by the calcined CoZn NPs is attributed to the external surface adsorption, which is different from the other adsorbing mechanism like the microporous adsorption process. Since an important fraction of the adsorption sites of the NPs is located in the exterior of the adsorbent compared with the porous adsorbent, it is easy for the adsorbate to access these active sites, thus resulting in a rapid approach to equilibrium. Additionally, it is clearly seen that the equilibrium time is a concentration-dependent parameter. It is very short for low Cr(VI) concentrations and increased gradually with the increase of concentration. For instance, the equilibrium time is of ~3 min for the concentration 20 mg L^{-1} and is of ~120 min for 100 mg L^{-1}. Further, the similar shape of the curves indicated that the removal efficiency increased inversely with the concentration of initial Cr(VI). This is expected because for a fixed adsorbent dosage, the total available adsorption sites are limited, thus leading to a decrease in percentage removal of the adsorbate. At equilibrium, the removal efficiency of Cr(VI) was found to vary between 100% and ~65% for the concentrations ranging from 20 to 100 mg L^{-1} (see the inset in Fig. 13). Therefore, the produced NPs are very promising for practical applications point of view. They showed better efficiency in contact with diluted wastewaters. From the study of the effect of adsorbent dose (see last section), we can expect that an appropriate adjustment of NP dose could further reduce the Cr(VI) concentration to the maximum allowable discharge limits. Environmentally, the allowable Cr(VI) dose depends on the medium in which the waste is discharged. It has been reported that in general, toxicity for most microorganisms occurs in the range of 0.05–5 mg chromium per kilogram of medium. Some aquatic species are more sensitive, and the allowable Cr(VI) dose is less than 10^{-2} mg L^{-1} [11]. Technologically speaking, we can expect that high reduction of Cr(VI) concentration could be achieved by subsequent treatment by passing the wastewater in a cascade system of magnetic NP beds appropriately mounted in the flow effluent. Then, efficient separation and retention of the NPs from the output-treated effluents could be readily achieved performing magnetic field-based separation techniques [52].

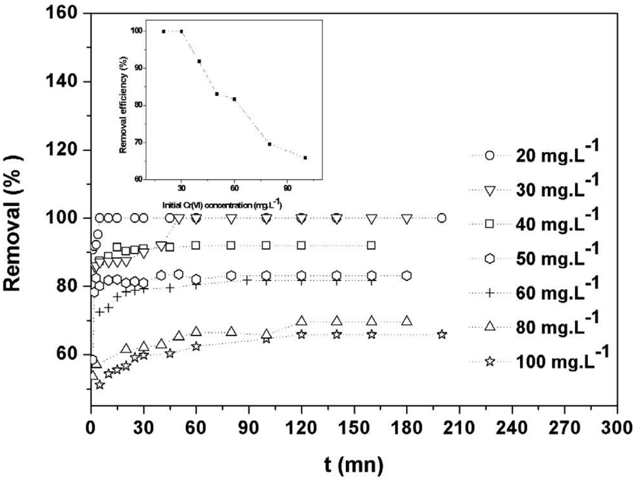

Fig. 13. Cr(VI) removal efficiency by the calcined CoZn NPs (4 g L^{-1}) as a function of contact time at various initial Cr(VI) concentrations. The inset depicts the removal percentage vs the initial Cr(VI) concentration at equilibrium state.

A number of adsorption kinetic models are known [53]. In our case, the best fit of adsorption data was found with the pseudo-second-order rate kinetic model. The integrated form of the pseudo-second order is expressed as:

$$\frac{t}{q_t} = \frac{1}{k_{\text{ad}} \times q_e^2} + \frac{t}{q_e} \tag{5}$$

where q_t and q_e refer to the adsorption capacities (mg g^{-1}) of the NPs at any time *t* (min) and at the equilibrium time, respectively. These quantities are calculated applying an equation like that of Eq. (5). The parameter k_{ad} (mg g^{-1} min^{-1}) refers to the adsorption rate constant. The Cr(VI) adsorption kinetic plots are presented in Fig. 14.

Parameters of pseudo-second order for Cr(VI) adsorption onto the calcined CoZn NPs along with the corresponding correlation coefficients (R^2) are summarized in Table 3.

The correlation coefficients for the linear plots t/q_t against *t* are very close to unity, and the q_e values ($q_{e,\text{cal}}$) calculated from pseudo-second-order model agree with the experimental values ($q_{e,\text{exp}}$) inferred from Fig. 14. The results indicated that the pseudo-second-order sorption mechanism is predominant for the sorption of Cr(VI) species onto our NPs, and it is considered that the rate of the sorption process is controlled by the chemisorption process. The mechanism involves valance forces through sharing or exchange of electrons between sorbent and sorbate as covalent forces [53]. In our case, the exchange of electrons of the NP surface and the Cr(VI) species is unfavorable for two reasons: (i) In all our experiments, chromium is dissolved in a strong oxidizing medium (HNO_3 10^{-2} M) in its highest oxidation state, +VI (as $K_2Cr_2O_7$ salt). (ii) Based on the well-known Pourbaix diagram of chromium [54], at room temperature and for pH 2.0, Cr is predominantly present in the form of $HCrO_4^-$ in which Cr is in the oxidation state +VI. These proofs excluded the transformation of Cr(VI) to Cr(III) and therefore excluded the presence of Cr(III) species in our hexachromium systems. Similar interpretation has also been reported by Hu et al. who demonstrated the absence of the trivalent Cr(III) in their hexavalent chromium-maghemite NP systems [28]. For our hexachromium-ferrite systems, the plausible mechanism involves the immobilization of Cr(VI) species on the NP surface as follows: At pH ~2.0 (far below the pH of the zero point of charge of spinel-type ferrites), the ferrite NPs are positively charged at their surface with the dominant $(OH_2)^+$ entities along with the cations of Fe^{3+}, Co^{2+}, and Zn^{2+} of the ferrite compound, while the Cr(VI) species are negatively charged, and they are predominantly present in the form of $HCrO_4^-$. This leads to an electrostatic attraction between the NP surface and the Cr(VI) species, and then the $HCrO_4^-$ species are chemisorbed on the NP surface via a chemical complexation mechanism to form surface coordination compounds as

$$\mathrm{M}^{z+} + \mathrm{HCrO}_4^- \rightarrow \left[\mathrm{M}^{(z-1)+}\mathrm{HCrO}_4\right] \tag{6}$$

where M^{z+} represents either Fe^{3+} or Co^{2+} species acting as Lewis acids (electron acceptors), while $HCrO_4^-$ entities acting as Lewis base (electron donor).

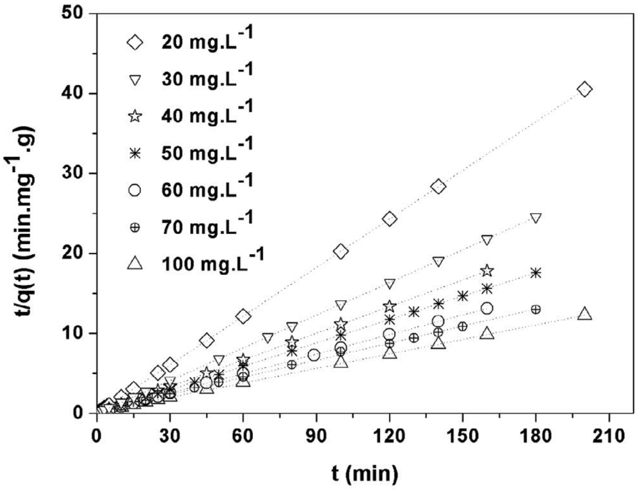

Fig. 14. Pseudo-second-order sorption kinetics of Cr(VI) species onto the calcined CoZn NPs (4 g L^{-1}) at various initial Cr(VI) concentrations. The dashed lines correspond to the best linear fit to the experimental data points.

It can be noticed from Table 3 that with the increase of the initial adsorbate concentration, the total amount of Cr(VI) adsorbed increased successively. This can be explained by the fact that more targets of Cr(VI) provide higher driving force to facilitate the ion diffusion from the solution to the positively charged NP surfaces and therefore more collisions between Cr(VI) ions and active sites of the sorbent [55].

3.4.4. Adsorption isotherms

The equilibrium data for the adsorption isotherms of Cr(VI) onto 4 g L^{-1} NPs are analyzed by the well-known Langmuir and Freundlich adsorption isotherm models [56,57]. Their respective linear Eqs. (7) and (8) are as follows:

$$\frac{C_e}{q_e} = \frac{C_e}{q_{\max}} + \frac{1}{b \times q_{\max}} \tag{7}$$

$$\ln(q_e) = \ln(k_f) + \frac{1}{n}\ln(C_e) \tag{8}$$

where the different parameters introduced in the above equations correspond to their usual meanings as defined by Langmuir and Freundlich. The values of the above-defined parameters are determined from the plot of C_e/q_e vs C_e and $\log(q_e)$ vs $\log(C_e)$ plots. The experimental data were treated by the Langmuir and Freundlich models (Fig. 15). As can be seen from Fig. 15(a), the adsorption data were satisfactorily fitted to the Langmuir model with $q_{\max}$ and *b* values of 15.6 mg g^{-1} and 0.15 L mg^{-1}, respectively. This suggests that the mechanism of adsorption is rather chemisorption than physical adsorption. For the Langmuir model, it is estimated by a dimensionless separation factor if the sorption is favorable or not. The separation factor, R_L, is calculated from the following relation:

$$R_L = \frac{1}{1 + bC_0} \tag{9}$$

Table 3
Parameters of pseudo-second order for Cr(VI) adsorption onto the calcined CoZn ferrite nanoparticles

Initial Cr(VI) concentration (mg L^{-1})	20	30	40	50	60	80	100
R^2	1.0	0.9990	1.0	0.9999	0.9900	0.9980	0.9997
Removal (%)	100	100	91.8	83.2	81.7	69.6	65.9
$q_{e,\mathrm{cal}}$ (mg g^{-1})	4.9	7.3	9.0	10.2	12.3	14.0	16.6
$q_{e,\mathrm{exp}}$ (mg g^{-1})	4.9	7.3	9.0	10.2	12.2	13.9	12.6
C_e (mg L^{-1})	0.0	0.0	8.1	16.8	18.3	30.4	34.1
K_{ad} (mg g^{-1} min^{-1})	2.43	0.85	0.37	0.33	0.076	0.022	0.018

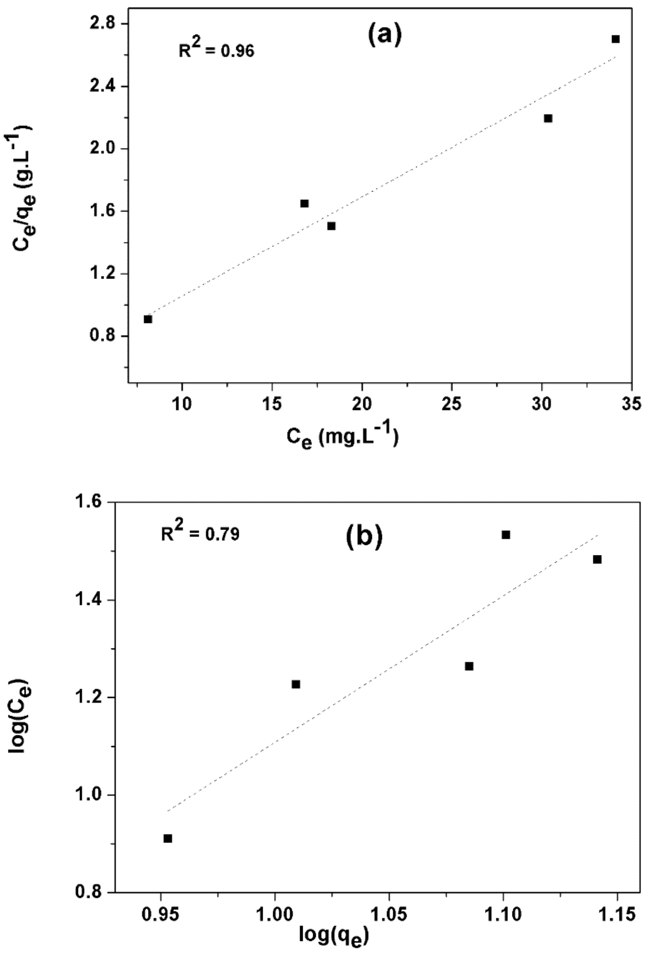

Fig. 15. Langmuir (a) and Freundlich (b) isotherms of Cr(VI) adsorption onto the calcined CoZn NPs (4 g L^{-1}) at various initial Cr(VI) concentrations. The dashed lines show the best fit of the experimental data points to the two models.

where the different parameters of Eq. (9) correspond to their usual meanings as defined by Langmuir and Freundlich. Values of R_L are found between zero and unity indicating that the sorption is favorable. In the present study, R_L lies in the range of 0.063 and 0.25, which demonstrated that the adsorption of Cr(VI) onto our moderately calcined NPs is feasible.

3.4.5. Reusability of the NPs

Adsorption–desorption–regeneration tests were conducted on a 15 mL Cr(VI) solution with an initial concentration of 80 mg L^{-1} and an NP dose of 4.0 g L^{-1}. To test the reusability of the nanoadsorbent, the following detailed procedure was adopted: In a first step, the NPs were shaked with the Cr(VI) solution for 30 min. Then, the absorbance of the supernatant was measured after decantation with the aid of NdFeB magnet. After this, to remove the adsorbed Cr(VI), the Cr(VI)-loaded NPs were dispersed in an excess (about 30 mL) of 0.5 M NaOH and then the mixture was sonicated for 5 min. Clearly, the supernatant shows the characteristic yellow color of water-soluble Cr(VI) entities. The last step was repeated until no detectable Cr(VI) was observed in the washing as confirmed by UV-Vis spectrum. The nanoadsorbent was then thoroughly washed with ultrapure deionizing water under sonication till the pH of the wash water became neutral. It is to be noticed that the supernatant appears colorless, indicating in particular the high chemical stability of our NPs; otherwise, redbrick color will appear due to the liberation of Fe^{3+} ion consequence of partial dissolution of the ferrite NPs. Then, the washed nanoadsorbent was dried at 60°C for 24 h to be reused for the subsequent adsorption–desorption–regeneration cycle as described above. Ten consecutive

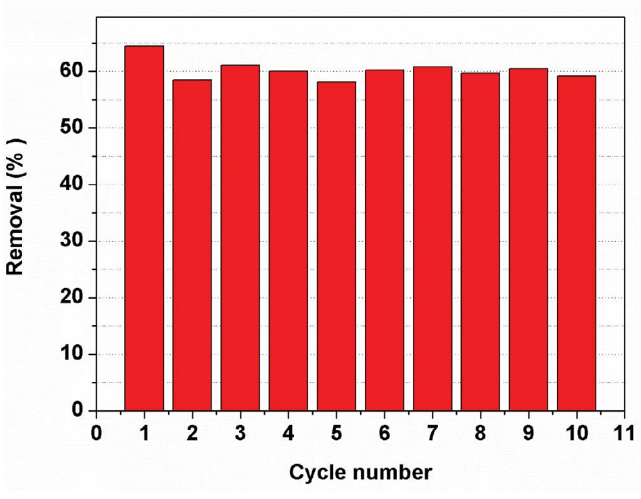

Fig. 16. Reusability of the calcined CoZn nanoadsorbent for adsorption–desorption of Cr(VI) during ten cycles. pH: 2.0; initial concentration of Cr(VI): 80 mg L^{-1}; NP dose: 4.0 g L^{-1}; contact time: 30 min; regenerating solution: NaOH 0.5 M.

adsorption–desorption–regeneration cycles were carried out to validate the reusability of the produced nanoferrite for the removal and recovery of Cr(VI). Fig. 16 shows the removal efficiency of Cr(VI) during ten cycles of adsorption–desorption–regeneration. As can be seen, a good reproducibility of the adsorption capacity (mean value » 61.0, standard deviation < 3) in the adsorption capacity of the nanoadsorbent during the ten cycles was achieved, which indicated that there were no irreversible adsorbent sites on the surface of the adsorbent. The results demonstrated that the moderately calcined CoZn nanoferrite can be used for the removal of Cr(VI) species over an important number of cycles, indicating its suitability for the design of a continuous process for the removal of Cr(VI)-bearing wastewaters.

4. Conclusion

The phase purity, the structure, the microstructure, the surface functionality, and magnetic properties of a new polyol-made CoZn nanoferrite and its moderately calcined one were investigated by various characterization techniques. EDX, XRD, and IR analyses showed that the as-produced powder and that obtained by moderate calcination of the former at 300°C are pure ultrasmall NPs with ~10 nm size possessing the chemical formula $Co_{0,6}Zn_{0,26}Fe_{2,09}O_4$. The two kinds of NPs exhibited a superparamagnetic behavior with reasonable saturation magnetization (M_{sat} (300 K): 64 and 70 emu g^{-1} for the calcined and the as-prepared, respectively) and high Curie temperature (T_C: 644 and 734 K for the as-prepared and the calcined, respectively). The interesting structural and magnetic properties make the produced nanoferrites good candidates for the removal of heavy metals from contaminated waters. Owing to its high chemical stability at pH 2.0, only the room temperature chromium (VI) adsorption capability study of the calcined nanocrystals was carried out. The Cr(VI) percent uptake was found to be strongly dependent on the NP dosage, the time, and the initial Cr(VI) concentration. It was shown that the adsorption phenomenon was rapid due to the greater number of active sites for interaction with chemical Cr(VI) species. Further, the equilibrium time is Cr(VI) concentration dependent; it increased with the increase of concentration. For instance, for an NP dose of 4.0 g L^{-1} and Cr(VI) concentrations varying between 20 and 100 mg L^{-1}, the equilibrium time was found to range between ~3 and ~120 min. Moreover, on the basis of the Langmuir isotherm model, the maximum uptake (q_{max}) of Cr(VI) was found to be at ~16 mg g^{-1} for an adsorbent dose of 4.0 mg mL^{-1}. These results showed that the moderately calcined NPs could potentially serve as nanoadsorbent of hexachromium, particularly by contact with low concentrated Cr(VI)-bearing liquid media. The nanoadsorbent was reused in ten adsorption–desorption cycles with negligible decrease in its sorption capacity, indicating in particular a highly chemically stable material. Thus, the moderately calcined CoZn nanoferrite has the potential to be used as an efficient and economic sorbent material for the removal of chromium (VI) from real wastewaters.

Acknowledgment

The authors are greatly indebted to the deanship of Scientific Research at Northern Border University for its funding of the present research work through the research project No. SCI-2017-1-7-F-6977.

References

[1] J. Ganoulis, Risk Analysis of Water Pollution, Wiley–VCH, Verlag GmbH & Co. KGaA, Weinheim, 2009.
[2] United Nations Environment Programme (Unep), Global Environment Outlook 2000, Earthscan Publications Ltd, UK, 1999.
[3] E. Laws, Aquatic Pollution: An Introductory Text, 4th Ed., John Wiley & Sons, New York, 2018.
[4] P.B. Chounwou, C.G. Yedjou, A.K. Patlolla, D.J. Sutton, in: A. Luch, Molecular, Clinical and Environmental Toxicology, Experientia Supplementum, Heavy Metal Toxicity and the Environment, Vol. 101, Springer, Basel, 2012, pp. 133–164.
[5] W.W. Eckenfelder, Industrial Water Pollution Control, 3rd Ed., McGraw-Hill Book Company, New York, 2000.
[6] I.A. Rodríguez, D.L.A. Rangel, J.F.C. González, M. de G.M. Zárate, V.M.M. Juárez, Hexavalent Chromium (VI) Removal by *Penicillium* sp. IA-01, N. Shiomi, Advances in Bioremediation of Wastewater and Polluted Soil, Intech, London, UK, 2015, pp. 165–191.
[7] T.L. Marsh, M.J. McInerney, Relationship of hydrogen bioavailability to chromate reduction in aquifer sediments, Appl. Environ. Microbiol., 67 (2001) 1517–1521.
[8] B. Marek, K. Nalan, L.R. Bernabé, J. Bundschuh, Sustainable water developments, Vol. 2, Innovative materials and methods for water treatment solutions for arsenic and chromium removal, CRC Press/Balkema, Taylor & Francis Group, London, UK, 2016.
[9] H. Seng, Y.T. Wang, Biological reduction of chromium by E. coli, J. Environ. Eng., 120 (1994) 560–572.
[10] D.E. Kimbrough, Y. Cohen, A.M. Winer, L. Creelman, C.A. Mabuni, Critical assessment of chromium in the environment, Crit. Rev. Environ. Sci. Technol., 29 (1999) 1–46.
[11] European Commission DG ENV. E3 Project ENV.E.3/ETU/2000/0058, Heavy Metals in Waste Final Report, February 2002.
[12] I. Ali, New Generation Adsorbents, Chem. Rev., 112 (2012) 5073–5091.
[13] T. Bora, J. Dutta, Applications of nanotechnology in wastewater treatment, J Nanosci. Nanotechnol., 14 (2014) 613–626.
[14] X. Qu, P.J.J. Alvarez, Q. Li, Applications of nanotechnology in water and wastewater treatment, Water Res., 47 (2013) 3931–3946.
[15] A. Roy, J. Bhattacharya, Nanotechnology in industrial wastewater treatment, IWP Publishing, London, UK, 2015.
[16] N.N. Nassar, The Application of Nanoparticles for Wastewater Remediation, B.V.D. Bruggen Ed., Applications of Nanomaterials for Water Quality, Future Science, London, UK, 2013.
[17] D.K. Tiwari, J. Behari, P. Sen, Application of nanoparticles in waste water treatment, World Appl. Sci. J., 3 (2008) 417–433.
[18] H.S. Samanta, R. Das, C. Bhattachajee, Influence of nanoparticles for wastewater treatment: a short review, Austin Chem Eng., 3 (2016) 1036–1041.
[19] P. Xu, G.M. Zeng, D.L. Huang, C.L. Feng, S. Hu, M.H. Zhao, C. Lai, Z. Wei, C. Huang, G.X. Xie, Z.F. Liu, Use of iron oxide nanomaterials in wastewater treatment: a review, Sci. Total Environ., 424 (2012) 1–10.
[20] M. Hua, S. Zhang, B. Pan, W. Zhang, L. Lv, Q. Zhang, Heavy metal removal from water/wastewater by nanosized metal oxides: a review, J. Hazard. Mater., 211–212 (2012) 317–331.
[21] H. Lu, J. Wang, M. Stoller, T. Wang, Y. Bao, H. Hao, An overview of nanomaterials for water and wastewater treatment, Adv. Mater. Sci. Eng., Vol. 2016, Article ID 4964828, 10 pages.
[22] Y.R. Zhang, S.Q. Wang, S.L. Shen, B.X. Zhao, A novel water treatment magnetic nanomaterial for removal of anionic and cationic dyes under severe condition, Chem. Eng. J., 233 (2013) 258–264.
[23] Y.C. Sharma, V. Srivastava, V.K. Singh, S.N. Kaul, C.H. Weng, Nano-adsorbents for the removal of metallic pollutants from water and wastewater, Environ. Technol., 30 (2009) 583–609.

[24] K.R. Kunduru, M. Nazarkovsky, S. Farah, R.P. Pawar, A. Basu, A.J. Domb, in: M.G. Alexandru, Water Purification Nanotechnology in the Agri-Food Industry, Academic Press, An imprint of Elsevier, Massachusetts, Cambridge, USA, 2017, pp. 33–74.

[25] L.B. Tahar, M.H. Oueslati, M.J.A. Abualreish, Synthesis of magnetite derivatives nanoparticles and their application for the removal of chromium (VI) from aqueous solutions, J. Colloid Interface Sci., 512 (2018) 115–126.

[26] J. Hu, G.H. Chen, I.M.C. Lo, Selective removal of heavy metals from industrial wastewater using maghemite nanoparticle: performance and mechanisms, J. Environ. Eng.,-ASCE, 132 (2006) 709–715.

[27] W. Weilong, F. Xiaobo, Efficient removal of Cr(VI) with Fe/Mn mixed metal oxide nanocomposites synthesized by a grinding method, J. Nanomater, Vol. 2013, Article ID 514917, 8 pages.

[28] J. Hu, G. Chen, I.M.C. Lo, Removal and recovery of Cr(VI) from wastewater by maghemite nanoparticles, Water Res., 39 (2005) 4528–4536.

[29] J. Hu, I.M.C. Lo, G. Chen, Fast Removal and Recovery of Cr(VI) using surface–modified jacobsite ($MnFe_2O_4$) nanoparticles, Langmuir, 21 (2005) 11173–11179.

[30] F. Fiévet, R. Brayner, in: R. Brayner, F. Fiévet, T. Coradin, Nanomaterials: A Danger or a Promise?, Springer, London, 2013, pp. 1–25.

[31] H. Huili, S. Nowak, L.B. Tahar, Polyol-made stoichiometric $Co_{0.2}Ni_{0.3}Zn_{0.5}Fe_2O_4$ nanoparticles: synthetic optimization, structural, and microstructural studies, Int. J. Nanotechnol., 12 (2015) 63–641.

[32] M. Artus, L.B. Tahar, F. Herbst, L. Smiri, F. Villain, N. Yaacoub, J.M. Grenèche, S. Ammar, F. Fiévet, Size-dependent magnetic properties of $CoFe_2O_4$ nanoparticles prepared in polyol, J. Phys.: Condens. Matter, 23 (2011) 506001 (9pp).

[33] A. Le Bail, Monte Carlo indexing with McMaille, Powder Diffract., 19 (2004) 249–254.

[34] H.M. Rietveld, A profile refinement method for nuclear and magnetic structures, J. Appl. Crystallogr., 2 (1969) 65–71.

[35] J.R. Carvajal, FullProf computer program, 2009. http://www.ill.eu/sites/fullprof/ (accessed January 2010).

[36] C. Suranarayana, M.G. Norton, X-ray Diffraction: A Practical Approach, Springer US, New York, 1998.

[37] L.B. Tahar, H. Basti, F. Herbst, L.S. Smiri, J.P. Quisefit, N. Yaacoub, J.M. Grenèche, S. Ammar, $Co_{1-x}Zn_xFe_2O_4$ ($0 \le x \le 1$) nanocrystalline solid solution prepared by the polyol method: characterization and magnetic properties, Mater. Res. Bull., 47 (2012) 2590–2598.

[38] H. Gleiter, Nanostructured materials: basic concepts and microstructure, Acta Materialia, 48 (2000) 1–29

[39] G.A. Petitt, D.W. Forester, Mössbauer study of cobalt-zinc ferrites, Phys. Rev. B., 4 (1971) 3912–3923.

[40] R.D. Waldron, Infrared spectra of ferrites, Phys. Rev., 99 (1955) 1727–1735.

[41] A.J. Rondinone, A.C.S. Samia, Z.J. Zhang, Control of the size of cobalt ferrite magnetic fluid, J. Phys. Chem. B, 103 (1999) 6876–6880.

[42] S.A. Makhlouf, F.T. Parker, A.E. Berkowitz, Magnetic hysteresis anomalies in ferritin, Phys. Rev. B, 55 (1997) 14717–14720.

[43] E.C. Stoner, E.P. Wohlfarth, A mechanism of magnetic hysteresis in heterogeneous alloy, Philos Trans R Soc A, 240 (1948) 599–642.

[44] Q. Song, Z.J. Zhang, Correlation between spin-orbital coupling and the superparamagnetic properties in magnetite and cobalt ferrite spinel nanocrystals, J. Phys. Chem. B, 110 (2006) 11205–11209.

[45] J. Smit, H.P.J. Wijn, Ferrites, Philips Technical Library, Eindhoven, Netherland, 1959.

[46] L. Néel, Influence des fluctuations thermiques sur l'aimantation de grains ferromagnétiques très fins, C.R. Acad. Sci., 228 (1949) 664–671.

[47] S. Cojocaru, Magnon gas and deviation from the Bloch law in a nanoscale Heisenberg ferromagnet, Phylos. Mag., 91 (2011) 4053–4062.

[48] A.K. Haghi, A.K. Zachariah, N. Kalarikkal, Nanomaterials: Synthesis, Characterization, and Applications, CRC Press, Boca Raton, USA, 2013.

[49] H. Huili, B. Grindi, A. Kouki, G. Viau, L.B. Tahar, Effect of sintering conditions on the structural, electrical, and magnetic properties of nanosized $Co_{0.2}Ni_{0.3}Zn_{0.5}Fe_2O_4$, Ceramics Int., 41 (2015) 6212–6225.

[50] J. Pradhan, S.N. Das, R.S. Thakur, Adsorption of hexavalent chromium from aqueous solution by using activated red mud, J. Colloid Interf. Sci., 217 (1999) 137–141.

[51] V.K. Gupta, A. Rastogi, Sorption and desorption studies of chromium(VI) from nonviable cyanobacterium *Nostoc muscorum* biomass, J. Hazard. Mater., 154 (2008) 347–354.

[52] J.R. Stephens, J.S. Beveridge, M.E. Williams, Analytical methods for separating and isolating magnetic nanoparticles, Phys. Chem. Chem. Phys., 14 (2012) 3280–3289.

[53] Y.S. Ho, G. McKay, Pseudo-second-order model for sorption processes, Process Biochem., 34 (1999) 451–465.

[54] B. Beverskog, I. Puigdomenech, Revised Pourbaix diagrams for chromium at 25°C–300°C, Corrosion Sci., 39 (1997) 43–57.

[55] J. Gong, X. Wang, X. Shao, S. Yuan, C. Yang, X. Hu, Adsorption of heavy metal ions by hierarchically structured magnetite–carbonaceous spheres, Talanta, 101 (2012) 45–52.

[56] I. Langmuir, The adsorption of gases on plane surfaces of glass, mica and platinum, J. Am. Chem. Soc., 40 (1918) 1361–1403.

[57] H.M.F. Freundlich, Über die adsorption in lösungen, Ind. Eng. Chem. Fundam., 57 (1906) 385–470.